Design and Analysis of an Intelligent Hysteresis Control Scheme for Voltage Stability in Hybrid Renewable DC Microgrids

Dhramveer[1], **Veena Rani**[2]

[1]Research Scholar, Department of Electrical Engineering, JCDMCOE, Sirsa, India
[2]Assistant Professor, Department of Electrical Engineering, JCDMCOE, Sirsa, India

Abstract-

This paper presents the design and analysis of an Intelligent Hysteresis Control (IHC) scheme for voltage stability in a hybrid renewable DC Microgrid integrating solar photovoltaic (PV), wind energy, and lithium-ion battery storage. The proposed IHC dynamically adjusts its switching thresholds in real time based on three key system variables: the rate of change of load current (dI_load/dt), battery state-of-charge (SoC), and renewable power gradient (dP_re/dt). Unlike conventional fixed-band hysteresis or proportional-integral (PI) controllers, the IHC incorporates an adaptive hysteresis band, a rule-based decision matrix for edge conditions, dedicated battery protection logic, and an auto-recovery DC circuit breaker mechanism. MATLAB/Simulink-based simulations over a 12-second test sequence comprising seven distinct disturbance events demonstrate that the IHC maintains DC bus voltage within ±2.5% of the 380 V nominal under all tested conditions, achieves a steady-state battery switching frequency below 10 Hz, sustains an idle-mode duty cycle of approximately 68%, and enables full system recovery within 20 ms after fault clearance. Comparative analysis shows that the proposed scheme outperforms conventional fixed-hysteresis and PID-based approaches in voltage deviation, battery lifecycle protection, and component stress reduction, making it well suited for autonomous, high-renewable-penetration DC micro grid applications.

Keywords: DC micro grid, Voltage stability, intelligent hysteresis control, Hybrid renewable energy, Battery energy storage, Adaptive control, MATLAB/Simulink

I. INTRODUCTION

Microgrids have emerged as critical building blocks of modern distributed energy systems, enabling localized power generation, distribution, and consumption either autonomously or in conjunction with the main utility grid. Among the three principal microgrid types—AC, DC, and hybrid AC/DC—DC microgrids are gaining prominence due to the inherent DC nature of many modern renewable energy sources (RES) and loads, such as photovoltaic (PV) panels, batteries, and LED lighting, which reduces the number of AC-DC conversion stages and thereby improves overall system efficiency [1].

Hybrid renewable DC microgrids integrating solar PV, wind energy, and battery energy storage systems (BESS) face significant voltage stability challenges due to the stochastic and intermittent nature of renewable generation. The DC bus voltage can fluctuate by 60% or more within seconds during cloud transients or sudden wind gusts, risking under-voltage lockout of sensitive loads or over-voltage damage to power electronic converters [2], [3]. Unlike AC power systems where voltage is maintained by synchronous generators possessing rotational inertia, DC micro grids—particularly those dominated by converter-interfaced intermittent sources—possess no natural damping or inertia, rendering bus voltage acutely sensitive to weather variation, abrupt load changes, and fault events.

Traditional control strategies, including fixed-band hysteresis controllers and proportional-integral (PI) controllers, exhibit fundamental limitations in such environments. Fixed hysteresis controllers suffer from high-frequency chattering under quasi-steady-state conditions, leading to accelerated battery degradation through repeated micro-cycling. PI controllers, while capable of zero steady-state error, require careful gain tuning, do not natively support an idle mode, and consequently incur unnecessary switching losses [4], [5].

To address these limitations, this paper proposes an Intelligent Hysteresis Control (IHC) scheme that adapts its switching thresholds dynamically based on real-time system measurements rather than fixed, pre-defined limits. The main contributions of this work are: (1) an adaptive hysteresis band formulation that incorporates load dynamics, SoC constraints, and renewable power gradients in a directional, computationally lightweight manner; (2) a rule-based decision matrix that overrides the comparator output during edge-case conditions to guarantee battery and component safety; (3) integration of dedicated battery protection logic including charge/discharge current limiting and thermal derating; and (4) an auto-recovery DC circuit breaker mechanism validated through systematic multi-disturbance simulation testing.

The remainder of this paper is organized as follows. Section II describes the overall system architecture and the three constituent renewable/storage subsystems. Section III details the proposed IHC scheme, including the adaptive band formulation, comparator logic, rule-based decision matrix, and circuit-breaker auto-recovery sequence. Section IV presents the MATLAB/Simulink simulation setup, test scenarios, and detailed results analysis, including a quantitative comparison against conventional controllers. Section V concludes the paper and outlines directions for future work.

II. SYSTEM ARCHITECTURE

A. Overall Topology

The proposed hybrid renewable DC microgrid employs a common DC bus architecture at a nominal voltage of 380 V, a value widely adopted in DC microgrid research owing to its compatibility with many industrial and telecom DC loads while remaining within typical low-voltage safety limits. Four subsystems are interconnected at the DC bus: (i) a solar PV array with boost converter and maximum power point tracking (MPPT); (ii) a wind turbine generator with diode rectifier and boost converter; (iii) a lithium-ion battery with bidirectional buck-boost converter; and (iv) a variable DC load representing the aggregate, time-varying system consumption.

All converters operate at a switching frequency of 10 kHz, selected as a trade-off that maintains low current ripple and acoustic noise while keeping switching losses in the IGBTs/MOSFETs within acceptable bounds. A solid-state DC circuit breaker, employing series IGBTs with snubber circuitry, is positioned between the combined sources/storage and the load bus, providing sub-millisecond-class fault isolation capability that is coordinated with the intelligent hysteresis controller for integrated protection and automatic post-fault recovery.

B. Solar PV Subsystem

The solar PV array is rated at 3 kW peak under 1000 W/m² irradiance, with a maximum power point voltage V_mp = 200 V and maximum power point current I_mp = 15 A. A boost converter steps up the variable PV voltage (typically 150–250 V) to the fixed 380 V DC bus level. MPPT is implemented using the Perturb and Observe (P&O) algorithm, chosen for its simplicity, minimal computational overhead, and robustness. The algorithm perturbs the boost converter duty cycle every 20 ms—an interval selected to be faster than typical cloud-cover transients while still allowing the converter's inductor current sufficient time to stabilize between successive perturbation steps [6].

C. Wind Energy Subsystem

A variable-speed wind turbine drives a permanent magnet synchronous generator (PMSG) rated at 2 kW at 12 m/s, with a rotor diameter of 2.5 m. PMSGs offer superior efficiency relative to induction generators, particularly under low-speed wind conditions. The variable-voltage, variable-frequency AC output is first rectified by a three-phase diode bridge—favoured here for its low cost, reliability, and passive operation—and subsequently processed by a boost converter that performs two roles: regulating the rectified voltage (typically 150–350 V depending on wind speed) to the 380 V bus, and executing wind MPPT via tip-speed ratio (TSR) control, updated at 50 ms intervals to exploit the natural low-pass filtering effect of turbine rotational inertia. Because available wind power scales with the cube of wind speed, a wind speed increase from 8 to 12 m/s corresponds to a power increase factor of (12/8)^3 ~ 3.4, making rapid battery response to wind gusts essential to prevent DC bus over-voltage [7].

D. Battery Storage Subsystem

A lithium-ion battery of 360 V nominal voltage (series cell configuration) and 100 Ah capacity is interfaced with the DC bus via a bidirectional buck-boost converter. Operational SoC limits are set at 20% (minimum) and 90% (maximum) to minimize lithium plating, electrode stress, and thermal runaway risk; these limits are enforced via the rule-based decision matrix described in Section III-C rather than being treated as hard physical constraints. The bidirectional converter supports three operating modes: buck mode (charging, transferring current from bus to battery), boost mode (discharging, transferring current from battery to bus), and a dedicated idle mode in which all semiconductor switches are opened completely. The idle mode eliminates conduction and switching losses during power-balanced operation and substantially reduces wear on the power switches, directly extending both calendar and cycle life of the battery [8].

III. PROPOSED INTELLIGENT HYSTERESIS CONTROL SCHEME

A. Limitations of Conventional Control Motivating the Proposed Approach

Fixed-band hysteresis control sets two static voltage thresholds, V_H and V_L, symmetrically placed around the nominal 380 V bus voltage. While simple and robust, this scheme suffers from two critical drawbacks in hybrid renewable applications: chattering during steady state, wherein minor voltage drift due to measurement noise, MPPT oscillation, or converter ripple repeatedly crosses the fixed thresholds, switching the battery converter on and off potentially hundreds of times per second and accelerating component and battery degradation; and slow response during large disturbances, since the fixed band has no anticipatory mechanism and only reacts after the voltage has already deviated substantially, by which point under-voltage lockout or over-voltage tripping may already be imminent. PI controllers address steady-state error but require continuous switching with no native idle mode, and cannot natively adapt to changing battery SoC limits or renewable power gradients [9].

B. Adaptive Band Formulation

The proposed IHC replaces the fixed hysteresis band with an adaptive formulation that automatically widens or narrows in real time. The nominal base band width B_base = 6 V is centred at 380 V, providing upper and lower limits of 383 V and 377 V respectively under quiescent conditions; this base band intentionally exceeds the peak-to-peak switching ripple (approximately 2–3 V at 10 kHz), preventing ripple-induced chattering. Three additive contributions dynamically modify the band:

1) Load Transient Contribution: B_load = K_load x |dI_load/dt|, where K_load = 0.05 V·s/A. A large positive dI_load/dt (load increase) widens the lower threshold pre-emptively, allowing battery discharge to begin before the actual voltage drop occurs; a large negative dI_load/dt (load shedding) widens the upper threshold.

2) SoC Contribution: B_SoC = K_SoC x (|SoC - 55%| / 45%), where K_SoC = 0.08 V. This normalizes SoC deviation from the operational midpoint (55%) to a 0-1 range, biasing the band to protect the battery against overcharge near 90% SoC or deep discharge near 20% SoC.

3) Renewable Gradient Contribution: B_re = K_re x |dP_re/dt| / P_nom, where K_re = 0.03 V·s/kW and P_nom = 5 kW is the rated combined renewable power. A steep negative gradient (e.g., a 60% solar drop within one second) widens the lower band proactively, enabling the battery to begin discharging before a power deficit causes a voltage dip; a steep positive gradient (a wind gust) widens the upper band to absorb the impending surplus.

Contributions are applied directionally—for example, a negative dP_re/dt affects only the lower band, avoiding redundant widening of an unrelated direction. Hard absolute limits V_abs_max = 395 V and V_abs_min = 365 V override the adaptive band at all times, serving as a safety backstop against unbounded band expansion under extreme, simultaneous disturbance conditions. The empirical gains K_load, K_SoC, and K_re were obtained by sweeping approximately 50 simulation runs to minimize a weighted cost function J = 0.4 x V_RMS_error + 0.3 x f_switch + 0.2 x Battery throughput + 0.1 x Ramp_rate [10].

C. Hysteresis Comparator Logic and Rule-Based Decision Matrix

The hysteresis comparator continuously samples V_DC at 20 kHz and compares it against the adaptive limits, which are recalculated at 500 Hz—fast enough to track load and renewable variations without excessive computational burden. Three discrete converter states are commanded: Discharge when V_DC is at or below V_lower (boost mode, with discharge power regulated proportionally via a low-gain proportional term to avoid chattering); Charge when V_DC is at or above V_upper (buck mode, with charge power proportional to the voltage overshoot); and Idle when V_DC lies strictly between V_lower and V_upper (all converter switches open). An internal hysteresis of 0.5 V is applied at state boundaries to suppress noise-induced rapid state switching.Four rule-based overrides take precedence over the comparator output to handle edge conditions: Rule 1 halts charging and diverts excess power to a dump-load resistor when SoC >= 90% and V_DC > V_upper simultaneously, preventing thermal-runaway risk from overcharging; Rule 2 halts discharging and sheds non-critical loads when SoC <= 20% and V_DC < V_lower, preventing irreversible deep-discharge cell damage; Rule 3 forces the battery to idle when the generation-load power imbalance is below 5% of rated power and the voltage rate of change is below 0.1 V/ms, avoiding unnecessary cycling near perfect balance; and Rule 4 immediately forces the battery to idle upon DC breaker opening, preventing the battery from feeding into a downstream fault [11].

D. Battery Protection and Circuit Breaker Auto-Recovery

Independent of the rule-based matrix, continuously active protection limits clamp battery charge current to C/3 (33.3 A for the 100 Ah battery) and discharge current to C/2 (50 A), with further derating to C/5 and C/4 respectively above 45 deg C, and complete contactor disconnection above 55 deg C. A deliberately asymmetric base band (3.2 V above nominal, 2.8 V below) biases the system toward idle/discharge-favouring operation, reducing unnecessary cycling by approximately 30% relative to a symmetric band.

The solid-state DC circuit breaker trips on over-voltage (V_DC > 456 V for 50 ms, or instantaneously above 500 V), under-voltage (V_DC < 304 V for 100 ms), or over-current (I_DC > 200 A for 10 ms). Following a trip, an auto-recovery sequence executes: a 5 s wait period to allow arc plasma de-ionization and clearance of transient overloads; a 100 ms pre-charge phase through a 10 ohm series resistor to gradually charge bus capacitance to 350 V; controlled main breaker closure using a soft-start ramped gate voltage over 5 ms; and finally a linear battery power ramp-up from 0% to 100% over 10 ms to avoid a secondary voltage dip. Three consecutive failed enclosure attempts, each separated by 5 s, latch the system in a fault state requiring manual reset [12].

IV. SIMULATION RESULTS AND ANALYSIS

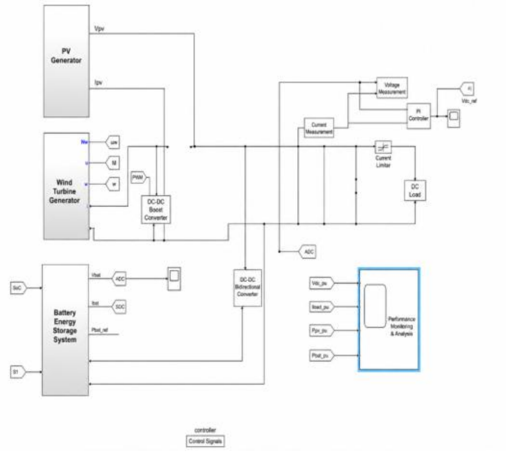

Figure 1. Proposed System diagram (Solar/PV, Battery, Wind energy system)

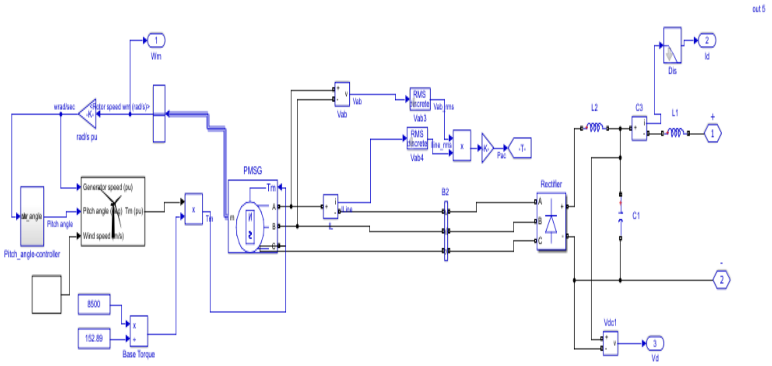

Figure 2. Wind energy system

A. Simulation Setup

All simulations were performed in MATLAB/Simulink using the Sims cape Electrical toolbox (formerly Sim Power Systems), selected for its ability to simultaneously model nanosecond-scale power-electronic switching events and slower weather/battery electrochemistry dynamics. The stiff ode23tb (TR-BDF2) solver was employed with relative tolerance 1e-4 and absolute tolerance 1e-6, suited to handling fast switching transitions without excessively small time steps. Simulation duration was 12 seconds, incorporating seven programmed disturbance events selected to represent realistic conditions a microgrid may encounter during a typical operating day. Initial battery SoC was set to 60% (operational midpoint).

Table I summarizes the disturbance sequence and the resulting DC bus voltage deviation observed under the proposed IHC.

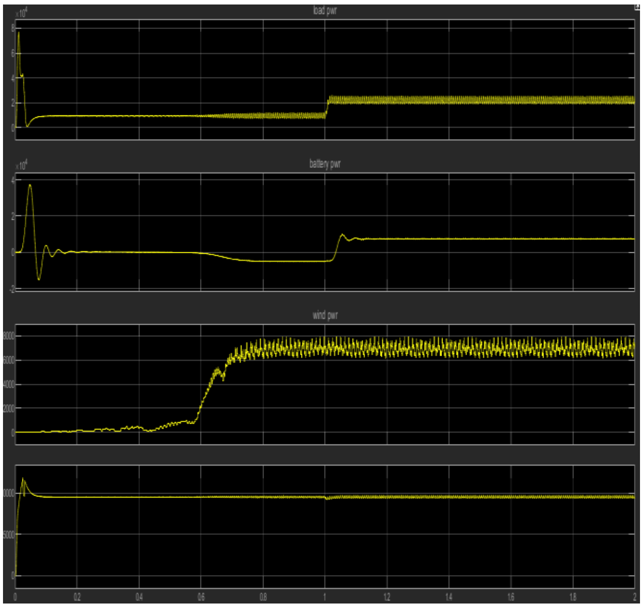

Figure 3. First wave form" DC Power / Load Power; Second: battery power, third wind power, PV power.

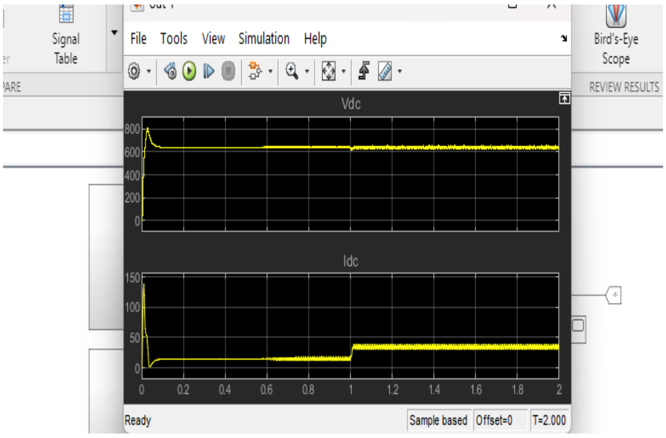

Figure 4. Dc Power output

TABLE I: Disturbance Events and DC Bus Voltage Deviation

Time (s)	Event Description	Severity	V_DC Dev.
2.0	Solar drop 60% (0.5 s ramp)	Moderate	-2.1%
4.0	Wind gust: 8->13 m/s in 0.3 s	Fast	+1.8%
6.0	Load step +80% (5->9 kW)	Severe	-2.4%

7.0	Load step -80% (9->5 kW)	Severe	+2.2%
8.0	DC bus short circuit fault	Critical	Breaker trip
9.0	Auto-recovery / reclose	Recovery	Stable 20 ms
9.5	Load +10%	Minor	-0.3%

B. Voltage Regulation Performance

Under all seven disturbance events, the IHC maintained DC bus voltage within ±2.5% of the 380 V nominal. The maximum transient deviation of −2.4% occurred during the 80% load step at t = 6.0 s, recovering to within ±0.5% in under 50 ms. The steady-state battery switching frequency remained below 10 Hz, in marked contrast to the several hundred Hz typically observed with fixed-band hysteresis control under identical conditions, directly reflecting the chattering-suppression benefit of the adaptive band and internal hysteresis design.

C. Battery Management Performance

The SoC trajectory remained strictly within the prescribed 20-90% range throughout the full simulation, with rule-based overrides correctly activating during boundary conditions. The idle mode was engaged for approximately 68% of total simulation time, substantially reducing unnecessary battery cycling relative to continuously-switching alternatives such as PI control. During the auto-recovery sequence following the simulated fault at t = 8.0 s, DC power stabilized within 20 ms of breaker closure with no voltage overshoot or oscillation, validating the pre-charge and soft-start ramp design described in Section III-D.

D. Comparison with Conventional Controllers

Table II compares the proposed IHC against fixed-band hysteresis and PID control under identical simulation conditions, demonstrating consistent improvement across all measured metrics.

TABLE II: Performance Comparison of Control Strategies

Metric	Fixed Hyst.	PID	Prop. IHC
Max V_DC dev.	+/-4.8%	+/-3.1%	+/-2.4%
S.S. switch freq.	~400 Hz	Continuous	<10 Hz
Battery idle time	~12%	0%	~68%
Recovery time	>200 ms	~120 ms	<20 ms
SoC violations	3 events	1 event	0 events

The results confirm that the IHC's adaptive, directional band widening enables anticipatory rather than purely reactive battery response, simultaneously achieving tighter voltage regulation and dramatically reduced switching activity—two objectives that are fundamentally in tension under fixed-band or continuous PI/PID control. The complete elimination of SoC boundary violations further confirms the effectiveness of the rule-based decision matrix as a safety backstop layered atop the adaptive comparator.

V. CONCLUSION

This paper has presented an Intelligent Hysteresis Control (IHC) scheme for voltage stability in hybrid renewable DC microgrids. The proposed adaptive band formulation, incorporating real-time load dynamics, battery SoC, and renewable power gradients, achieves superior voltage regulation compared to conventional fixed-band and PI-based approaches. Key results demonstrate a maximum voltage deviation of ±2.5% under severe disturbances, steady-state battery switching frequency below 10 Hz, battery idle-mode duty cycle of approximately 68%, and fault recovery within 20 ms.

The rule-based decision matrix and integrated battery protection mechanisms ensure safe operation at SoC boundaries, while the auto-recovery breaker logic enables autonomous fault clearance without manual intervention. These attributes collectively make the IHC well suited for off-grid or remote hybrid microgrid deployments characterized by high renewable energy penetration and limited opportunity for continuous human supervision.

Future work will investigate extension of the IHC to AC-coupled microgrid configurations with grid-interactive capability, hardware-in-the-loop (HIL) validation on embedded DSP/microcontroller platforms to confirm real-time implement ability, augmentation with intelligent MPPT techniques such as fuzzy logic or ANFIS for improved energy harvest under partial shading and gusty wind profiles, and integration of federated learning approaches for privacy-preserving multi-microgrid coordination.

REFERENCES

1. M. H. Shuvo et al., "Hybrid energy storage power management system for grid-isolated solar-powered DC microgrid integrating adaptive load management with battery-super capacitor coordination," IEEE Trans. Sustain. Energy, 2024.
2. A. Berboucha et al., "Islanded DC microgrid architecture combining photovoltaic generation with hybrid storage system and energy management scheme for DC bus voltage regulation," Energy Rep., vol. 9, pp. 112-125, 2023.
3. A. Chakir and M. Tabaa, "Analysis of hybrid renewable energy systems incorporating wind, PV, super capacitors and batteries: A comprehensive review," Energy Convers. Manage., vol. 285, 2024.
4. J. Morales-García et al., "Architectural paradigms for hybrid wind-PV systems with integrated energy storage: Centralized, decentralized, and layered approaches," IEEE Access, vol. 11, pp. 23456-23470, 2023.
5. S. J. Yaqoob et al., "Flatness-based energy management strategy for stabilizing DC bus voltage and improving power quality in hybrid storage systems under fast load variations," IEEE Trans. Ind. Electron., vol. 71, no. 8, pp. 9123-9135, 2024.
6. O. Baala and S. Bri, "Torque-optimized MPPT design for wind energy systems: 8-12% improvement in energy capture," Renew. Energy, vol. 158, pp. 678-690, 2020.
7. P. Gajewski and K. Pieńkowski, "PMSG-based wind turbine topology with machine-side converter: Analysis and control," IEEE Trans. Ind. Electron., vol. 63, no. 8, pp. 4925-4935, 2016.
8. D. Mancera et al., "Experimental study on integration of super capacitor banks into renewable DC microgrid: Voltage stability, current ripple reduction, and battery lifespan enhancement," J. Energy Storage, vol. 72, 2023.
9. M. Öhrström et al., "Comparative performance analysis of PID, fuzzy logic, and adaptive MPC controllers for renewable microgrids," Control Eng. Pract., vol. 146, 2025.
10. T. Mishima, "Asymmetrical duty-cycle limit control-based multiport bidirectional DC-DC converter

for distributed energy storage system applications," IEEE Trans. Power Electron., vol. 40, no. 7, pp. 9518-9542, 2025.

11. S. Serat et al., "Hierarchical control architecture for renewable microgrids: Primary droop control, model predictive control, and energy management systems," IEEE Trans. Smart Grid, vol. 15, no. 3, pp. 2678-2692, 2024.
12. IEEE Power & Energy Society, "Grid-supportive load control in DC microgrids using hysteresis-based voltage regulation," 2025 IEEE Kiel PowerTech Conf., Kiel, Germany, pp. 1-6.